Neurobiology of Disease

Amyloid Pathology Impairs Experience-Dependent Inhibitory Synaptic Plasticity

Suraj Niraula,[1] Shirley ShiDu Yan,[1,2] and Jaichandar Subramanian[1]

[1]Department of Pharmacology and Toxicology, School of Pharmacy, University of Kansas, Lawrence, Kansas 66045 and [2]Department of Surgery, Vagelos College of Physicians and Surgeons of Columbia University, New York, New York 10032

Alzheimer's disease patients and mouse models exhibit aberrant neuronal activity and altered excitatory-to-inhibitory synaptic ratio. Using multicolor two-photon microscopy, we test how amyloid pathology alters the structural dynamics of excitatory and inhibitory synapses and their adaptation to altered visual experience in vivo in the visual cortex. We show that the baseline dynamics of mature excitatory synapses and their adaptation to visual deprivation are not altered in amyloidosis. Likewise, the baseline dynamics of inhibitory synapses are not affected. In contrast, visual deprivation fails to induce inhibitory synapse loss in amyloidosis, a phenomenon observed in nonpathological conditions. Intriguingly, inhibitory synapse loss associated with visual deprivation in nonpathological mice is accompanied by subtle broadening of spontaneous but not visually evoked calcium transients. However, such broadening does not manifest in the context of amyloidosis. We also show that excitatory and inhibitory synapse loss is locally clustered under the nonpathological state. In contrast, a fraction of synapse loss is not locally clustered in amyloidosis, indicating an impairment in inhibitory synapse adaptation to changes in excitatory synaptic activity.

Key words: **Alzheimer's disease; clustered synaptic plasticity; homeostatic plasticity; in vivo imaging; inhibitory synapse; neuronal hyperactivity**

Significance Statement

Using multicolor in vivo two-photon microscopy to capture high-resolution images of excitatory and inhibitory synapses from the same neurons over time, we show that amyloid pathology selectively disrupts experience-dependent adaptation of inhibitory synapses. Furthermore, our findings reveal that local clustering of excitatory and inhibitory synapse loss is disrupted, a deficit that could underlie impaired neuronal activity homeostasis, and plasticity in AD.

Introduction

Coordination of excitation and inhibition governs the activity of cortical neurons and shapes computation (Isaacson and Scanziani, 2011). Neuronal hyperactivity has been observed early in Alzheimer's disease (AD) patients and mouse models, suggesting impaired neuronal activity homeostasis (Busche and Konnerth, 2016; Palop and Mucke, 2016; Frere and Slutsky, 2018). Functional magnetic resonance imaging studies have found hyperactivity of cortical and hippocampal regions in patients with mild cognitive impairment and pre-symptomatic individuals with a predisposition to AD (Targa Dias Anastacio et al., 2022), indicating neuronal hyperactivity is an early feature in some AD patients. As the disease progresses, hyperactivity transitions to hypoactivity (O'Brien et al., 2010).

Mouse models of AD also exhibit neuronal hyperactivity (Busche and Konnerth, 2016; Palop and Mucke, 2016), but interestingly, hyper- and hypoactive neurons are present at the same time (Busche et al., 2008). We also recently found that a small fraction of neurons in the visual cortex of hAPP mice show higher responsiveness and a larger fraction of neurons are nonresponsive to natural image stimuli compared to nonpathological mice (Niraula et al., 2023). Hyper- and hypoactive neurons in amyloidosis indicate that changes to activity levels may not trigger compensatory synaptic plasticity mechanisms. This failure may stem from multiple causes, such as impaired detection of excitability changes, or if they are detected, the subsequent response, mediated through synaptic plasticity mechanisms, is impaired (Styr and Slutsky, 2018).

Inhibitory synaptic plasticity is one of the compensatory adaptations to changes in excitatory drive (Gainey and Feldman, 2017; Chen et al., 2022). Postmortem tissues of AD

Received April 19, 2023; revised Nov. 9, 2023; accepted Nov. 14, 2023.

Author contributions: S.S.Y. and J.S. designed research; S.N. performed research; S.S.Y. contributed unpublished reagents/analytic tools; S.N. and J.S. analyzed data; J.S. wrote the paper.

This work was supported by a grant from the National Institutes of Health (Grant No. RO1AG064067) to J.S. and 1RF1AG081575 to S.Y. and J.S. We thank the members of the Subramanian Lab for their comments on the manuscript. We thank Don Arnold (USC) for providing GPHN.FingR-GFP-expressing virus.

The authors declare no competing financial interests.

Correspondence should be addressed to Jaichandar Subramanian at jaichandar@ku.edu.

https://doi.org/10.1523/JNEUROSCI.0702-23.2023

patients exhibit synapse loss, with many studies, but not all, showing a reduction in excitatory or inhibitory synapses (Melgosa-Ecenarro et al., 2023). Contradictory findings regarding the early involvement of inhibitory synapses in AD pathogenesis are also observed in various mouse models of the disease (Melgosa-Ecenarro et al., 2023). It is unclear whether inhibitory synapse plasticity and their adaptation to changes in excitatory drive are altered in AD-associated pathology.

Structural synaptic adaptations to changes in neural activity patterns in vivo are typically studied in sensory cortices by altering sensory experience-evoked activity (Gainey and Feldman, 2017; Lee and Kirkwood, 2019). Under nonpathological conditions, sensory deprivation leads to structural plasticity of excitatory and inhibitory synapses, favoring increased excitability of adult cortical neurons in vivo. For instance, visual deprivation increases the strength and size of excitatory synapses in the visual cortex and modulates their dynamics (Goel and Lee, 2007; Keck et al., 2008, 2013; Hofer et al., 2009; Coleman et al., 2010; Barnes et al., 2017; Zhou et al., 2017; Sammons et al., 2018; Sun et al., 2019). In addition, adult layer 2/3 neurons exhibit increased loss of inhibitory synapses following visual deprivation (Keck et al., 2011; Chen et al., 2012; van Versendaal et al., 2012; Villa et al., 2016; Niraula et al., 2023), and mature excitatory synapses become less dynamic (Subramanian et al., 2019).

In vivo multiphoton imaging of structural synaptic dynamics in mouse models of AD thus far is limited to dendritic spines and axonal boutons (Liebscher and Meyer-Luehmann, 2012; Dorostkar et al., 2015; Subramanian et al., 2020). These studies reveal increased synaptic dynamics favoring their loss, particularly closer to amyloid plaques, though the phenotype varies depending on the age, mouse strain, or the brain regions examined (Subramanian et al., 2020). How amyloid disrupts inhibitory synapses is less understood and remains controversial (Jimenez-Balado and Eich, 2021; Melgosa-Ecenarro et al., 2023). Though amyloid accumulates in the boutons of inhibitory neurons (Kurucu et al., 2022), the basal structural dynamics of these boutons are not significantly altered (Ruiter et al., 2021). However, some studies but not others have found axonal degeneration of inhibitory neurons and structural synapse loss (Garcia-Marin et al., 2009; Palop et al., 2011; Mitew et al., 2013; Kiss et al., 2016; Schmid et al., 2016; Umeda et al., 2017; Hollnagel et al., 2019; Petrache et al., 2019; Ruiter et al., 2020; Shimojo et al., 2020; Sos et al., 2020; Montero-Crespo et al., 2021; Kurucu et al., 2022; Niraula et al., 2023; Scaduto et al., 2023). A challenge to studying inhibitory postsynaptic dynamics in vivo is that they are primarily present in the dendritic shaft of excitatory neurons and lack a morphological surrogate, such as dendritic spines, which are typically used as a proxy for excitatory synapses. However, most dynamic spines carry immature excitatory synapses (Villa et al., 2016; Vardalaki et al., 2022); therefore, how amyloid influences mature excitatory synapse dynamics in vivo remains unclear. Whether amyloid pathology disrupts the experience-dependent structural plasticity of mature excitatory or inhibitory synapses in vivo is also unclear.

Using a synaptic labeling approach that reliably detects mature excitatory and inhibitory synapses of cortical neurons and in vivo multicolor two-photon imaging, we show that the baseline dynamics of mature excitatory and inhibitory synapses are not altered in the visual cortex of a mouse model of AD [hAPP mice—J20 line (Harris et al., 2010)]. Interestingly, visual deprivation-evoked structural loss of inhibitory synapses is disrupted in these mice. In contrast, reduced excitatory synaptic dynamics associated with visual deprivation are preserved, indicating that neurons in amyloid pathology retain their ability to sense changes in experience-evoked excitability. Accompanying inhibitory synapse loss, we also observe the broadening of spontaneous but not visually evoked calcium transients selectively in nonpathological mice. We show that impaired structural adaptation of inhibitory synapses following visual deprivation could stem from the impaired local coupling of excitation and inhibition, manifested as a reduced spatial clustering of the loss of excitatory and inhibitory synapses.

Methods

Mice. The University of Kansas Institute of Animal Use and Care Committee has authorized all animal procedures and complies with the NIH standards for the use and care of vertebrate animals. Transgenic hAPP mice overexpressing a mutant human form of amyloid precursor protein (APP) that encodes hAPP695, hAPP751, and hAPP770 bearing mutations linked to familial AD [APPV717F (Indiana), KM670/671NL (Swedish)], J-20 line were obtained from Jackson Laboratory. J20 mice and wild-type (WT) females from the same background were bred to generate heterozygotes for the hAPP transgene. J20 males and C57BL/6J-Tg (Thy1-GCaMP6s) GP4.3Dkim/J [strain 024275, JAX (Chen et al., 2013)] females were bred to generate J20-GCaMP6s mice. Five mice at most were kept in a cage, but following cranial window surgery, they were individually housed on a 12 h light/dark cycle or 24 h darkness for visual deprivation experiments. Both genders were used in the study.

DNA constructs. The Cre-dependent TdTomato (pFudioTdTomato W), Teal-gephyrin (pFudioTealgephyrinW), and PSD-95-venus (pFudioPSD-95venusW) plasmids were a kind gift from Dr. Elly Nedivi. The pSIN-W-PGK-Cre plasmid was used to express Cre recombinase (Subramanian et al., 2013). The Cre-dependent expression of fluorescently labeled synaptic markers PSD-95 and gephyrin have been shown to accurately represent excitatory and inhibitory synapses, respectively (Villa et al., 2016).

In utero electroporation. Timed pregnancies were established between heterozygous J20 males and WT females with the same genetic background. Half of the litter was heterozygous for the APP transgene, while the other half was WT (control). Using a 32-gauge Hamilton syringe (Hamilton Company), plasmids diluted in 1 µl of Tris-EDTA (1:0.5:1:0.15 molar ratios of pFudioTdTomatoW, pFudioTealgephyrinW, pFudioPSD-95venusW, and pSIN-W-PGK-Cre, respectively) were injected in the lateral ventricle of E15.5 to E16.5 embryos. A square wave electroporator (ECM830, Harvard Apparatus) was used to deliver five pulses of 36 V (50 ms duration at 1 Hz) to a pair of platinum electrodes (Protech International) targeted at the visual cortex.

Cranial window. A cranial window was placed in 4–6-month-old J20 and WT mice over the visual cortex in the right hemisphere. An incision was made above the midline of the skull. The pericranium was softly scraped, and soft tissues were displaced laterally by blunt dissection. A biopsy punch was used to score a 5-mm-diameter circle covering the visual cortex. Using a fine drill and a sterile 0.5-mm-diameter round burr (Fine Science Tools), the skull was thinned along the scored circle. Fine forceps were used to carefully remove the bone flap, leaving the dura intact. A sterile, 5-mm-diameter circular glass coverslip (Harvard Apparatus) was placed over the opening. To secure the coverslips in place, firm pressure was applied while Vetbond was placed over the area where the coverslip and bone met. Over the exposed skull, Metabond (C&B Metabond) was placed, and a titanium head post was attached to the window about 2 weeks following the surgery.

Viral injections. For GCaMP6s expression, we used pAAV.syn.GCaMP6s.WPRE.SV40 (viral titer/ml, 1.3×10^{13}; Addgene 100843-AAV9).

For jRGECO and GPHN.FingR.EGFP expression, we used pAAV.Syn.NES-jRGECO1a.WPRE.SV40 (viral titer/ml, 3.2×10^{13}; Addgene 100854-AAV9), pCAG.DIO.GPHN.FingR.EGFP2F (viral titer/ml, 2.4×10^{13}; a kind gift from Don Arnold), and pENN.AAV.CamKII 0.4.Cre.SV40 (viral titer/ml, 2.3×10^{13} GC/ml; Addgene 105558-AAV9) in the ratio 2:1:1, respectively. We injected the viruses in the right primary visual cortex in three locations centered on stereotactic coordinates 2.9 mm lateral and 0.5 mm anterior to lambda. We injected at a depth of 150–300 μm from the dura and 150 nl per injection site at the rate of 25–30 nl/min. The needle was slowly retracted after 5 min of the injection on each site, and a cranial window encompassing the viral injection sites was placed.

Optical intrinsic signal imaging. Approximately 14 d after cranial window surgeries, optical intrinsic signal (OIS) imaging was performed to map the location of the visual cortex. A custom-designed upright microscope with a 4× objective (Nikon) was used for imaging. Mice were lightly sedated using isoflurane and positioned 20 cm in front of a high refresh rate monitor showing a horizontal bar drifting at 10 Hz. Images were captured at 5 Hz with an sCMOS camera (1,024 × 1,024 pixels; Photometrics). The cortex was illuminated (500–600 m below the dura) using 610 nm light delivered by a fiber-coupled LED controlled by T-Cube LED drivers (Thorlabs). A 470 nm light was used to image reference vasculature. Cortical intrinsic signals were computed by extracting the Fourier component of light reflectance changes to matched stimulus frequency from downsized images (256 × 256 pixels). The magnitude maps were thresholded at 30% of the peak response amplitude. The fractional change in reflectance represents response magnitude. The magnitude maps were superimposed over the 470 nm reference image to map the visual cortex.

Widefield calcium imaging. Instead of using intrinsic signal imaging to map the location of the visual cortex in GCaMP6s transgenic mice, widefield calcium imaging was employed. The mapping methodology was comparable to intrinsic signal imaging, except fluorescence was imaged as opposed to reflected light. GCaMP6 was excited by an LED (Lambda FLED, Sutter Instrument) filtered through a bandpass filter (470/40, 49002, Chroma Technology), and the emission was filtered with a 525/50 bandpass filter.

Two-photon imaging. Synaptic structural imaging was performed on isoflurane-anesthetized mice with sparsely labeled neurons in the mapped visual cortex using a Sutter MOM multiphoton microscope. The Ti:sapphire laser (MaiTai HP, 915 nm; Newport Spectra-Physics) was directed toward the microscope using table optics. A polarizing beam splitter and a rotating half-wave plate were used to regulate laser power. A pair of galvanometric mirrors scan the laser beams to the back aperture of the objective (Nikon 16× 0.8 NA). The output power from the objective was set to 40–50 mW. The same objective was used to gather the emission signal, which was then routed through appropriate bandpass filters (488/50, 540/50, and 617/73 for teal, Venus, and TdTomato fluorescence, respectively) and three GaASP PMTs. Image acquisition was controlled by ScanImage (Vidrio Technologies), and images were obtained at 0.16 Hz. The imaging field covered 133 × 133 × ∼150 μm (1,024 × 1,024 XY pixels, Z step, 1 μm).

For measuring calcium transients during visual deprivation, transgenic (3 WT, 2 hAPP mice) and virally delivered GCaMP6s (2 WT, 2 hAPP mice) were used. Neurons within the mapped visual cortex (∼100–150 μm below the dura) were imaged at 4.22 Hz in head-restrained awake mice restrained in a body tube. The excitation wavelength was set to 940 nm, and the power was adjusted to avoid signal saturation. The imaging field was a single Z frame of 336 × 336 μm (256 × 256 pixels) consisting of ∼50–100 cells. In each imaging session, we first imaged calcium transients in complete darkness (for spontaneous activity; 213 s), followed by visual stimuli (415 s). Visual stimuli consisted of six trials of three seconds of phase reversing orientation grating stimuli (0°, 30°, 60°, 90°, 120°, 150°) that do not drift and natural images. Six seconds of gray screen interspersed grating and natural image stimuli were presented in random order in each trial.

jRGECO imaging was restricted to spontaneous activity imaging and was performed similarly to GCaMP6 imaging, except that the excitation wavelength was set to 1,040 nm. Immediately following jRGECO imaging, mice were anesthetized and imaged for GPHN.FingR-GFP. The imaging field for gephyrin FingR-GFP covered 133 × 133 × 25 μm (1,024 × 1,024 XY pixels, Z step, 0.25 μm). The excitation wavelength was set to 915 nm. The power was adjusted to avoid signal saturation.

In vivo synaptic imaging analysis. The signal collected in each photomultiplier tube [(PMT) channel] is a combination of signals from the three fluorophores (teal, venus, and TdTomato) due to their overlapping emission spectra. We used spectral linear unmixing to reassign the signal from each fluorophore to the appropriate channel. Each image consisted of three channels: cell fill (TdTomato), PSD-95 (venus), and gephyrin (teal) channels. First, gephyrin and PSD-95 puncta were marked if they were present in two consecutive frames and consisted of at least 8–9 or 4–5 clustered pixels, respectively, in mean-filtered, volume-corrected images. For volume correction (normalization of the signal relative to local dendritic volume), we normalized the fluorescence in the synaptic channels to that of the cell fill channel. A normalization factor was calculated as the ratio of the mean pixel value of a chosen dendrite in the cell fill channel to the synaptic channel. Each pixel value in the synaptic channel was then multiplied by the normalization factor, and the pixel value of the cell fill channel was subtracted on a pixel-to-pixel basis. A custom-written 4D point tracking system implemented in Fiji using a modified version of the ObjectJ plugin (Villa et al., 2016) was used to transfer labeled markers (indicating each synapse type or no synapse) to matched locations on images from subsequent imaging sessions. Synaptic markers were transferred back to the identical location on the unmixed image for quantification. A custom-written macro was used to place a 5 × 5 pixel box [synaptic region of interest (ROI)] at the center of synaptic puncta for PSD-95 on the spines and shaft gephyrin. The box overlapped with part of both puncta for dually innervated spines containing both PSD-95 and gephyrin puncta. The 5 × 5 pixel boxes (background ROI) were also placed on dendritic shaft locations lacking visible puncta to calculate background fluorescence. The background ROI boxes, equaling the number of identified synapses, were placed along the entire length of the dendritic segment used for synapse identification. PSD-95 puncta on spines were classified as excitatory synapses based on a clustering index ($CI_{PSD\text{-}95}$), which is calculated as:

$$CI_{PSD95} = (F_{PSD95}/F_{cellfill})/(F_{bg\_PSD95}/F_{bg\_cellfill})$$

where $F_{PSD\text{-}95}$ and $F_{cellfill}$ are the mean fluorescence of synaptic ROI from PSD-95 and cell fill channel of an identified puncta, respectively, and $F_{bg\_PSD\text{-}95}$ and $F_{bg\_cellfill}$ are the mean + 3× standard deviation of fluorescence of the 10 nearest background ROIs to that puncta. Similarly, $CI_{gephyrin}$ is calculated as:

$$CI_{gephyrin} = F_{gephyrin}/F_{bg\_gephyrin}$$

where $F_{gephyrin}$ and $F_{cellfill}$ are the mean fluorescence of synaptic ROI and background ROI of the gephyrin channel, respectively. PSD-95 and gephyrin are considered excitatory and inhibitory synapses if their clustering index is greater than one.

The gain and loss of a specific type of synapse between sessions were determined by calculating the number of newly formed puncta or lost puncta of that synapse type and dividing it by the total number of puncta of that synapse type in the later or previous session, respectively.

For nearest neighbor distance analysis, we first calculated the cumulative distance along the trace of the dendrite generated by simple neurite tracer (SNT) by iteratively summing the Euclidean distances between consecutive points (XYZ coordinates) of the SNT trace. This creates a continuous distance measurement along the SNT trace. We then computed pairwise distances between each synapse marker and all points along the SNT trace using the Euclidean distance formula, considering

the 3D coordinates (X, Y, Z) of each marker and trace point. For each synapse marker, we identified the SNT trace point that is closest to it by finding the minimum distance from the pairwise distance calculations using the "pdist2" function. The distance of a synaptic puncta from the soma was calculated by summation of the distance of the puncta to the nearest SNT tracepoint and the distance from that point to the soma. To identify the nearest synapse, the distances of all synapses to each other were first calculated based on their distances from the soma, and the nearest synapse was determined using the "knnsearch" function in MATLAB.

The nearest neighbor of both excitatory and inhibitory dynamic synapses was calculated using a similar approach. To evaluate whether the observed spatial relationships between synapse losses on dendritic branches deviated from a random distribution, we used experimentally observed data on synaptic density, dendritic length, and the count of lost synapses for each dendritic segment. We also used the experimentally observed dendritic locations of "source" synapse losses, which act as reference points for identifying the closest "target" synapse losses. Using a custom-written code in MATLAB, we then generated random locations of target synapse losses and calculated the nearest neighbor distance. This process was repeated for each source synapse across all dendrites and averaged. We iterated it 10,000 times to generate a random distribution of nearest neighbor distances of lost target synapses to each lost source synapse.

We tracked 2,453 PSD-95$^+$ spines in WT mice, 2,156 in hAPP mice, 1,111 gephyrin puncta in WT, and 1,073 in hAPP mice across three imaging sessions. These structures were identified in 54 dendrites spanning a length of 4,133 µm in WT mice and 48 dendrites spanning 3,719 µm in hAPP mice. The synaptic density from the first imaging session for some of the analyzed hAPP neurons has been published (Niraula et al., 2023).

The objectJ plugin described above was also used to track gephyrin puncta identified by GPHN.FingR-GFP across sessions. A 5 × 5 ROI was placed over the identified puncta, and two additional ROIs were placed in the nearby background using a custom-written macro. Puncta were scored as gephyrin if the fluorescence was greater than three standard deviations from the mean of all background ROIs on the image and if the puncta was present in five consecutive imaging frames (0.25 µm/frame). We tracked 422 puncta from 6 WT mice.

Calcium imaging analysis. The data (Fig. 4*C*) on spontaneous calcium imaging is an independent analysis from the same raw data used for other analyses previously published (Niraula et al., 2023). Suite2p was used to perform motion registration, and ROI detection on the time-series images (Pachitariu et al., 2017) with tau was set at 2 s (GCaMP6s) or 0.7 s (for jRGECO). If the soma was discernible in the mean or maximum projection picture, ROIs generated by Suite2p were selected as cells (cellular ROI). The neuropil-corrected fluorescence (Fcorr) is calculated as F – (0.5 × Fneu). dF/F0 is calculated as (Fcorr – F0)/F0, where F0 is defined as the mode of the Fcorr density distribution. For each neuron, the mean dF/F0 over every 3 s was calculated for 228 s (76 × 3 s) and averaged. The percentage of neurons in each indicated dF/F0 bin was calculated as the number of neurons in that bin divided by the total number of identified neurons for each mouse. To assess functional connectivity in cellular ROIs obtained from Suite2p, we deconvolved spikes and applied a threshold (>2 SD from the mean) before binarizing the data. We then determined functional connections between pairs of neurons by comparing their coactive frames to a distribution generated from 1,000 random circular shifts of their activity. Neuron pairs with coactive frames exceeding the 95th percentile of this distribution were considered functionally connected. We used the resulting functional connectivity matrix to determine the node degree of each neuron, which represents the number of edges (or connections) connected to that node over the entire imaging period. We calculated node degrees using MATLAB's graph and degree functions.

To assess the area under each transient's curve (AUC), we set a threshold of mean plus two standard deviations of the entire spontaneous or visually evoked stimulus periods. We used MATLAB's "findpeaks" function to identify peaks, and the area under each peak above the threshold was calculated using the "trapz" function. The area of all the transients during the spontaneous imaging period was averaged for each neuron. We excluded the gray screen imaging frames from analysis for visually evoked calcium transients and averaged all transients across different stimuli for each neuron. Neurons were not matched between imaging sessions.

Statistics. Statistics were performed using MATLAB, SPSS, or GraphPad Prism. *p*-values and statistical procedures are provided in the figure legends. $p < 0.05$ is considered significant unless mentioned otherwise (for Bonferroni corrections). To compare the mean of the observed nearest distances of target and source synapse loss with that of randomly generated distribution, we obtained a left-sided *p*-value as the mean was always to the left of the random distribution.

Results

Selective disruption of experience-dependent structural plasticity of inhibitory synapses on the dendritic shaft in amyloid pathology

To study how amyloid pathology influences the dynamics of excitatory and inhibitory synapses in vivo, we used an in utero electroporation (IUE)-based synaptic labeling strategy that sparsely labels layer 2/3 cortical neurons in the visual cortex (Chen et al., 2012; Villa et al., 2016; Subramanian et al., 2019). Three fluorescent proteins, TdTomato (cell fill), PSD-95-venus (excitatory synaptic marker), and Teal-gephyrin (inhibitory synaptic marker), were expressed in a Cre recombinase dependent manner (Fig. 1*A*). Previous studies have shown that this approach reliably represents excitatory and inhibitory synapses in the same neurons in vivo along with dendritic spines (Chen et al., 2012; Villa et al., 2016). We used multicolor two-photon microscopy to image individual neurons expressing all fluorescent markers in the visual cortex in vivo under normal and visual deprivation conditions. Visual deprivation allows us to examine structural synaptic adaptation to reduced experience-evoked activity. To assess synaptic dynamics under baseline and altered experience conditions, we imaged the same neurons and synapses thrice with an interval of 7 d between imaging sessions (Fig. 1*A*,*B*). Between the first two imaging sessions, the mice were housed in a 12 h light/dark cycle (baseline). Immediately following the second imaging session, mice were transferred to 24 h darkness until the final imaging session (visual deprivation). The appearance of new synapses (gain) and disappearance of preexisting synapses (loss) between the first two imaging sessions represent baseline dynamics, and that between the second and third sessions includes changes associated with altered experience (Fig. 1*C*–*G*).

The synaptic labeling scheme allows us to detect four types of synaptic structures—dendritic spines with (PSD-95$^+$ spines) or without (PSD-95$^-$ spines) PSD-95, gephyrin on dendritic shaft (inhibitory shaft synapse), and gephyrin on PSD-95$^+$ spines (inhibitory spine synapse). To assess the dynamics of excitatory synapses and inhibitory synapses, we tracked the gain and loss of PSD-95$^+$ spines [2,453 (WT), 2,156 (hAPP)] and gephyrin on the shaft and spines [1,111 (WT), 1,073 (hAPP)]. The average excitatory (WT, 0.59 ± 0.04/µm; hAPP, 0.58 ± 0.04/µm) and inhibitory (WT, 0.27 ± 0.06/µm; hAPP, 0.28 ± 0.05/µm) synapse densities did not differ between the genotypes.

Under baseline conditions, the gain and loss of all synapse types were balanced. Approximately 2–3% of excitatory synapses were gained, and a similar fraction was lost during baseline conditions (Fig. 2*A*) for both WT and hAPP mice, indicating that amyloid pathology in the visual cortex prior to plaque does not

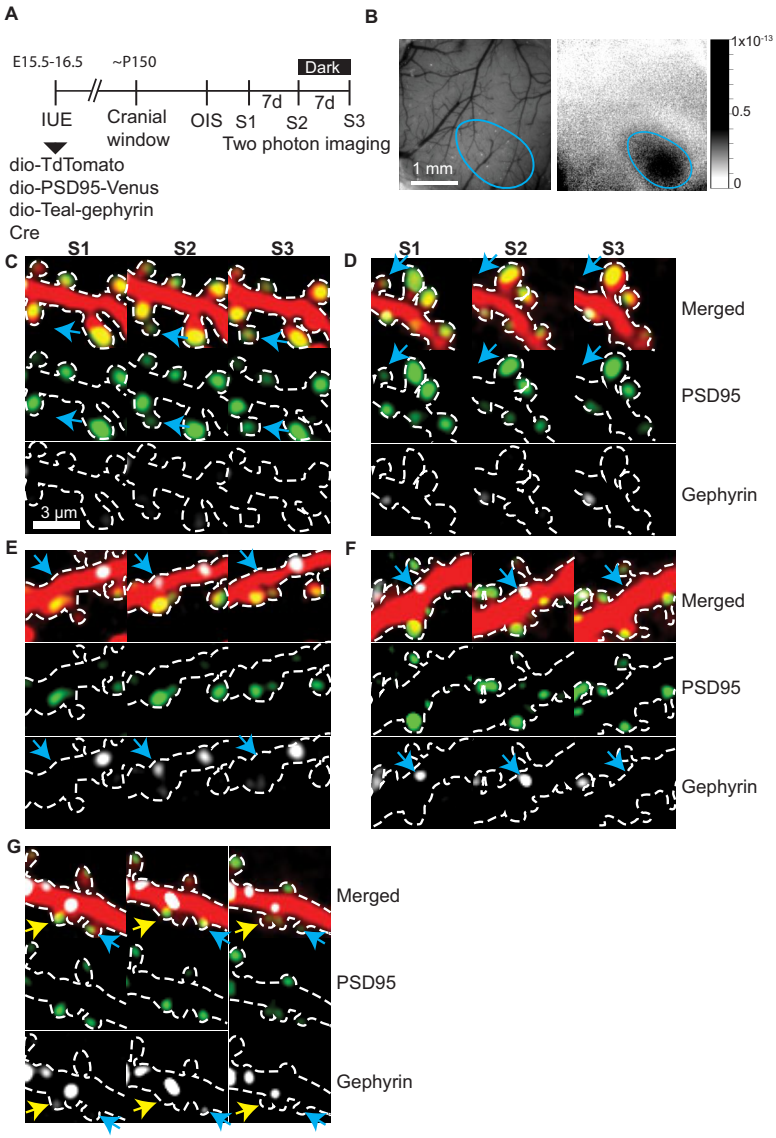

Figure 1. In vivo structural imaging of experience-dependent synaptic plasticity. ***A***, Timeline of imaging. IUE of plasmids expressing Cre recombinase and Cre-dependent markers was performed on embryonic days 15.5–16.5. A cranial window was placed at ~5 months old, and 2 weeks later, OIS imaging was performed to map the visual cortex. Two-photon imaging of neurons in the mapped visual cortex was performed in three imaging sessions (S1, S2, and S3). Each imaging session was separated by 1 week, and mice were housed in 24 h darkness (24 D) between S2 and S3. At all other times, they were housed under 12 h light/dark cycle. ***B***, A cranial window (left) and a magnitude map (blue oval) of intrinsic signal (right, grayscale bar indicates the change in reflectance normalized to baseline). ***C–G***, Pseudocolored images of the same dendritic segments from the three sessions (red, cell fill; green, PSD-95; gray, gephyrin). PSD-95 and gephyrin channels are shown below the merged images. Gain and loss (blue arrows (***C–F***) of excitatory synapses (gain, ***C***; loss, ***D***), inhibitory synapse on shaft (gain followed by loss, ***E***; loss, ***F***), and inhibitory synapses on spines (blue arrow, gain in S2 loss in S3; yellow arrow, loss, ***G***).

lead to increased loss of excitatory synapses. We found that visual deprivation reduced the gain of excitatory synapses in WT mice. A similar reduction in the gain of these synapses was also seen in hAPP mice (Fig. 2*A*). Overall, we observed a significant effect for light deprivation [$p < 0.01$; $F_{(1, 13)} = 15.06$; two-way mixed model ANOVA], but the effect was not significantly different between genotypes or the interaction of light and genotype. In contrast to the gain of excitatory synapses, the loss between two sessions did not differ significantly between genotypes or light conditions (remained between 2 and 3% across conditions; Fig. 2*A*). These results show that excitatory neurons adapt similarly to changes in visually evoked excitability under amyloid and nonpathological conditions.

Inhibitory synapses are more dynamic than excitatory synapses (Villa et al., 2016). Consistently, we found that ~11% of inhibitory shaft synapses were gained or lost under baseline conditions in WT mice (Fig. 2*B*). The gain and loss were slightly lower in hAPP mice under baseline conditions (~9% gain and ~7% loss; Fig. 2*B*), although it did not reach statistical significance. When visually evoked activity is reduced by visual deprivation, the gain of new inhibitory shaft synapses was reduced by 2–3% in both WT and hAPP mice. However, the effect is not significantly different between the genotypes, light conditions, or their interaction, indicating that pre-plaque amyloid pathology under baseline conditions does not affect the gain of new inhibitory shaft synapses.

Visual deprivation elicits disinhibition as a homeostatic adaptation under nonpathological conditions (Gainey and Feldman, 2017). At the structural level, the loss of inhibitory synapses is increased by visual deprivation in nonpathological mice (Chen

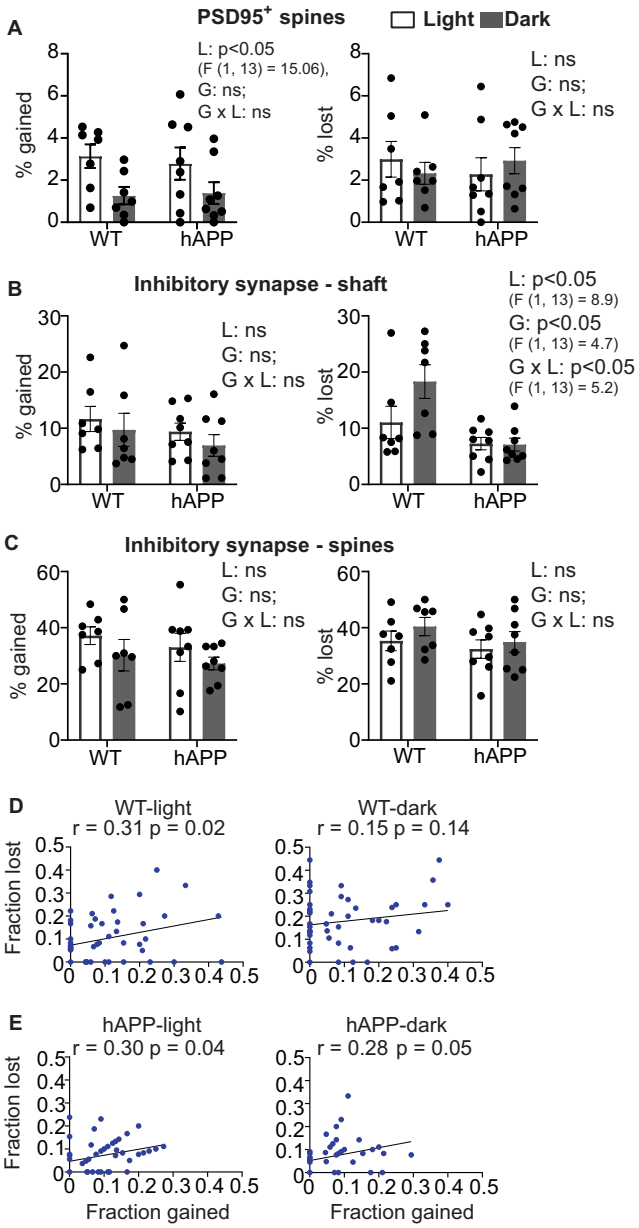

Figure 2. Inhibitory but not excitatory synaptic structural adaptation deficits in amyloid pathology. ***A–C***, Percentage of excitatory synapses (***A***), inhibitory synapses on shaft (***B***), and inhibitory synapses on spines (***C***) gained (left) or lost (right) in baseline (light) and visual deprivation (dark) conditions in wild-type (WT) and hAPP mice. Circles represent individual neuron values. $n = 7$ neurons (5 WT mice) and 8 neurons (7 hAPP mice). Two-way mixed model ANOVA was used to test the effect of light vs dark (L), genotype (G), and their interaction (G × L). ns, not significant. Data are presented as mean ± SEM. ***D***, ***E***, Correlation of percentage gain and loss of inhibitory shaft synapses on individual dendrites in WT (***D***) and hAPP (***E***) mice in baseline and visual deprivation conditions $n = 54$ dendrites (WT) and 48 dendrites (hAPP).

et al., 2012; van Versendaal et al., 2012). Consistently, we found that dark adaptation increased the loss of inhibitory shaft synapses by 63% in WT mice (18% loss; Fig. 2*B*). Interestingly, the loss of inhibitory shaft synapses remained identical (~7% loss) to baseline conditions in hAPP mice (Fig. 2*B*). Consequently, for inhibitory shaft synapses, we found a significant effect for genotype [$p < 0.05$, $F_{(1, 13)} = 8.918$], visual deprivation [$p < 0.05$, $F_{(1, 13)} = 4.733$], and their interaction [$p < 0.05$, $F_{(1, 13)} = 5.215$; two-way mixed model ANOVA; Fig. 2*B*]. Inhibitory synapses on spines are more dynamic than inhibitory shaft synapses (Chen et al., 2012; van Versendaal et al., 2012). Consistent with a previous study (Villa et al., 2016), we found that 30–40% of inhibitory synapses on spines were gained or lost under baseline conditions in both WT and hAPP mice (Fig. 2*C*). Though visual deprivation increased the net loss of inhibitory spine synapses [gain/loss, 1.05 (light), 0.75 (dark)] in WT mice, the effect was not different between genotypes, visual deprivation, or their interaction (Fig. 2*C*). These results show that amyloid pathology selectively disrupts the structural adaptation of inhibitory shaft synapses to loss of visual experience.

Since the average gain and loss of inhibitory shaft synapses were balanced under baseline conditions [gain/loss, 1.05 (light)], we tested whether this balance persisted at the level of individual dendrites. We found that the correlation between the gain and loss of inhibitory synapses on dendritic branches was significant in WT mice under baseline conditions (Fig. 2*D*). The correlation reduced during visual deprivation and was no longer significant (Fig. 2*D*). However, the difference in correlation between baseline and visual deprivation conditions was not significantly different ($p > 0.05$, Fisher r to z transformation). These results indicate that the gain and loss of inhibitory shaft synapses are balanced, and visual deprivation mildly disrupts this balance. The correlation between gain and loss remained close to significance in hAPP mice under both baseline and visual deprivation conditions, suggesting that amyloid does not disrupt the balance of gain and loss of inhibitory shaft synapses (Fig. 2*E*).

Different inhibitory neuron subtypes project to various dendritic locations. Parvalbumin-expressing interneurons innervate perisomatic and proximal (<40 µm from the soma) dendrites, whereas somatostatin-expressing neurons primarily project to distal dendrites (>40 µm from the soma; Di Cristo et al., 2004). Therefore, we examined whether visual deprivation-associated increase in the loss of inhibitory shaft synapses occur differentially depending on dendritic location, with some locations exhibiting higher synapse loss (hotspots). The density of inhibitory shaft synapses is the highest close to the soma and progressively decreases both in WT and hAPP mice (Fig. 3*A*,*B*). Visual deprivation uniformly and subtly reduces the density of inhibitory shaft synapses at different distances from the soma in WT mice (Fig. 3*A*). In hAPP mice, the density remained identical across all three sessions for all distances from the soma (Fig. 3*A*). Similarly, the increased loss of inhibitory shaft synapses in visual deprivation is evident at all distances from the soma in WT mice (Fig. 3*A*), whereas the loss of synapses was very similar in hAPP mice at all measured distances from the soma (Fig. 3*A*). These results indicate that there may be no dendritic hotspot for elevated inhibitory synapse loss.

A fraction of inhibitory synapses tend to appear and disappear at the same dendritic locations (Villa et al., 2016). To test whether the structural loss of inhibitory shaft synapses during visual deprivation was driven mainly by the loss of newly acquired or those present in both imaging sessions, we compared their relative contribution to the total inhibitory shaft synapse loss (Fig. 3*B*). Of the ~18% synapses that were lost in WT mice in the dark, only 3.6% of them were newly formed synapses in the second session, and the rest (14.8%) were synapses present in the first and second sessions (Fig. 3*C*). In hAPP mice, of the 7% of shaft synapses that were lost during visual deprivation, ~5% were present in both sessions, and 2% were newly gained synapses (Fig. 3*C*). The loss of newly gained synapses did not differ significantly; therefore, the synapses present in the first two sessions were more stable in hAPP mice (Fig. 3*C*).

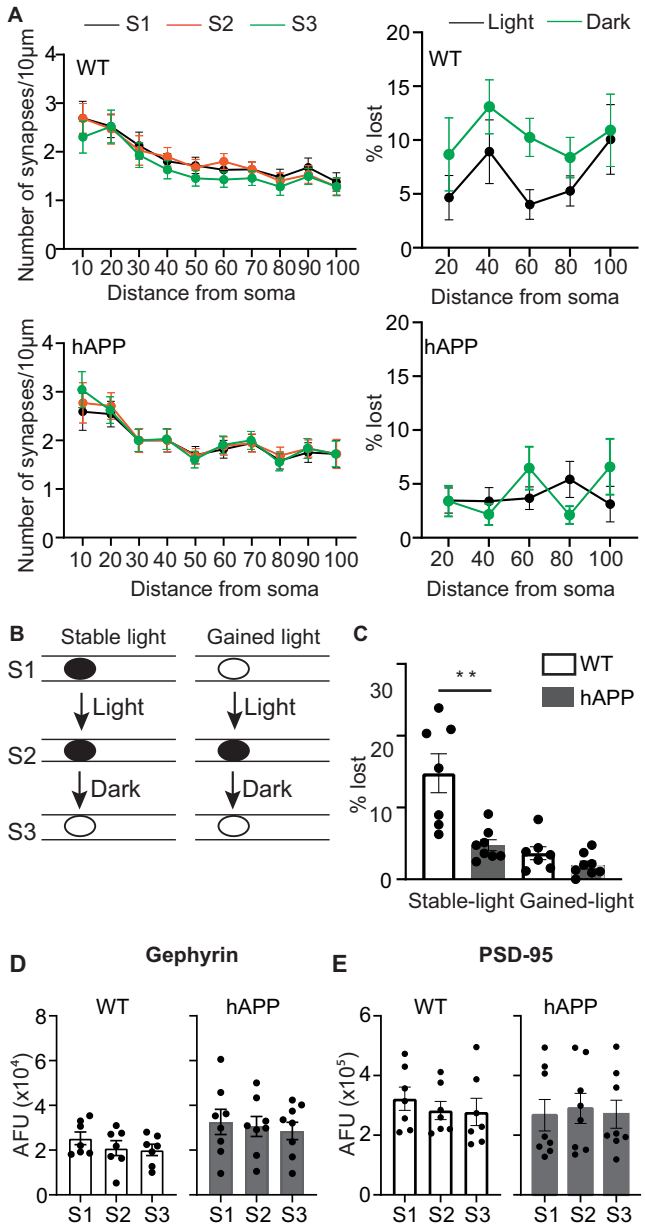

Figure 3. Characterization of inhibitory synapse loss on the dendritic shaft. ***A***, (Left) Density of inhibitory shaft synapses at different distances from soma from the three imaging sessions (S1, S2, and S3) in WT and hAPP mice. (Right) Percentage loss of inhibitory shaft synapses at different distances from the soma in baseline (light) and visual deprivation (dark) conditions in WT and hAPP mice. $n = 54$ dendrites (WT) and 48 dendrites (hAPP). ***B***, Representation of an inhibitory shaft synapse that was present in the first two imaging sessions (stable light) but was lost in the third session (left) and a synapse that appeared in the second imaging session (gained light) and disappeared (right). ***C***, Percentage of stable and gained inhibitory shaft synapses lost following visual deprivation (dark). $n = 7$ (WT) and 8 (hAPP) neurons. $^{**}p < 0.01$, $F_{(2,12)} = 7.2$; one-way multivariate ANOVA. ***D***, ***E***, Average fluorescence (arbitrary fluorescence units) of the inhibitory shaft (***D***) and mature excitatory (PSD-95; ***E***) synapses in the three sessions in WT and hAPP mice. Circles represent neuron values, and data are presented as mean ± SEM.

Since the size of gephyrin puncta correlates with the synaptic strength (Villa et al., 2016), we tested whether visual deprivation decreases the average fluorescence intensity of shaft synapses that remained stable across the three sessions. We found no difference in average gephyrin fluorescence between sessions in WT and hAPP mice (Fig. 3*D*). Visual deprivation increases dendritic spine size or gain in layer 5 neurons (Hofer et al., 2009; Keck et al., 2013; Barnes et al., 2017), indicating increased excitatory synaptic strength. To test whether excitatory synapse strength is altered by visual deprivation, we compared whether stable dendritic spines show changes in PSD-95 fluorescence, which correlates with synaptic strength (Fortin et al., 2014), following dark exposure. Consistent with studies that found no difference in spine size or gain in layer 2/3 neurons upon visual deprivation (Hofer et al., 2009; Barnes et al., 2015), we also found no significant difference in average PSD-95 fluorescence across sessions (Fig. 3*E*). Similar results were obtained when the gephyrin or PSD-95 fluorescence was normalized to the cell fill fluorescence (not shown).

Amyloidosis impacts changes in spontaneous activity associated with visual deprivation but not baseline activity

Since structural inhibitory synapse loss in the dendritic shaft is an adaptation triggered by decreased experience-evoked neural activity (Chen et al., 2012; van Versendaal et al., 2012), its disruption in hAPP mice could be due to increased baseline spontaneous neuronal activity in these mice compared to WT. Using calcium imaging, we previously found that average spontaneous population activity (mean population dF/F0 of GCaMP6 transients) in the visual cortex recorded without visual experience is not significantly different in ∼5–6-month-old hAPP mice (Niraula et al., 2023). However, the same average population activity may arise despite differences in the distribution of activity patterns and correlational structure. We analyzed this data set of spontaneous activity over ∼228 s from 1,020 WT and 885 hAPP neurons (Fig. 4*A*). To assess whether the distribution of neurons exhibiting distinct mean calcium responses [quantified as dF/F0 (%)] during spontaneous activity differed, we categorized neurons into various bins based on their mean dF/F0 values. We found that the activity distribution is similar between the genotypes (Fig. 4*A*).

The activity of a neuron is sensitive to the correlation of their inputs (Salinas and Sejnowski, 2001), and therefore, we tested the possibility that changes to the correlational structure of spontaneous neural activity may underlie impaired inhibitory synapse loss in hAPP mice. We obtained the mean correlation for each animal by averaging all the individual neuron–neuron correlations. We found that WT and hAPP mice had a similar average correlation (Fig. 4*B*). The amplitude of individual calcium transients could be influenced by the number of coactive neurons (node degrees), even when the average calcium transient levels are similar between genotypes. We calculated the node degree of a neuron as the number of significant coactive neurons. Two neurons are considered significantly coactive if the number of imaging frames these neurons are coactive is greater than 95% of the cumulative distribution of coactivity generated by 1,000 random circular shifts of activities between two neurons. Again, we found no difference in the average node degree of WT and hAPP mice (Fig. 4*C*). Consistently, the mean AUC of individual calcium transients was also similar between the genotypes (WT, 7.5 ± 0.27, hAPP: 7.03 ± 0.19). These results indicate that baseline spontaneous neuronal activity is not altered in amyloidosis.

To test whether differential effects of visual deprivation on inhibitory synapse loss in WT and hAPP mice also manifest at the neural activity level, we imaged spontaneous and visually evoked calcium transients in the same mice over three imaging sessions, with each imaging session separated by 1 week. Mice were housed in complete darkness between the second and third sessions (Fig. 4*D*, i). In each session, we imaged spontaneous and visually evoked (stimulus consists of phase reversing orientation

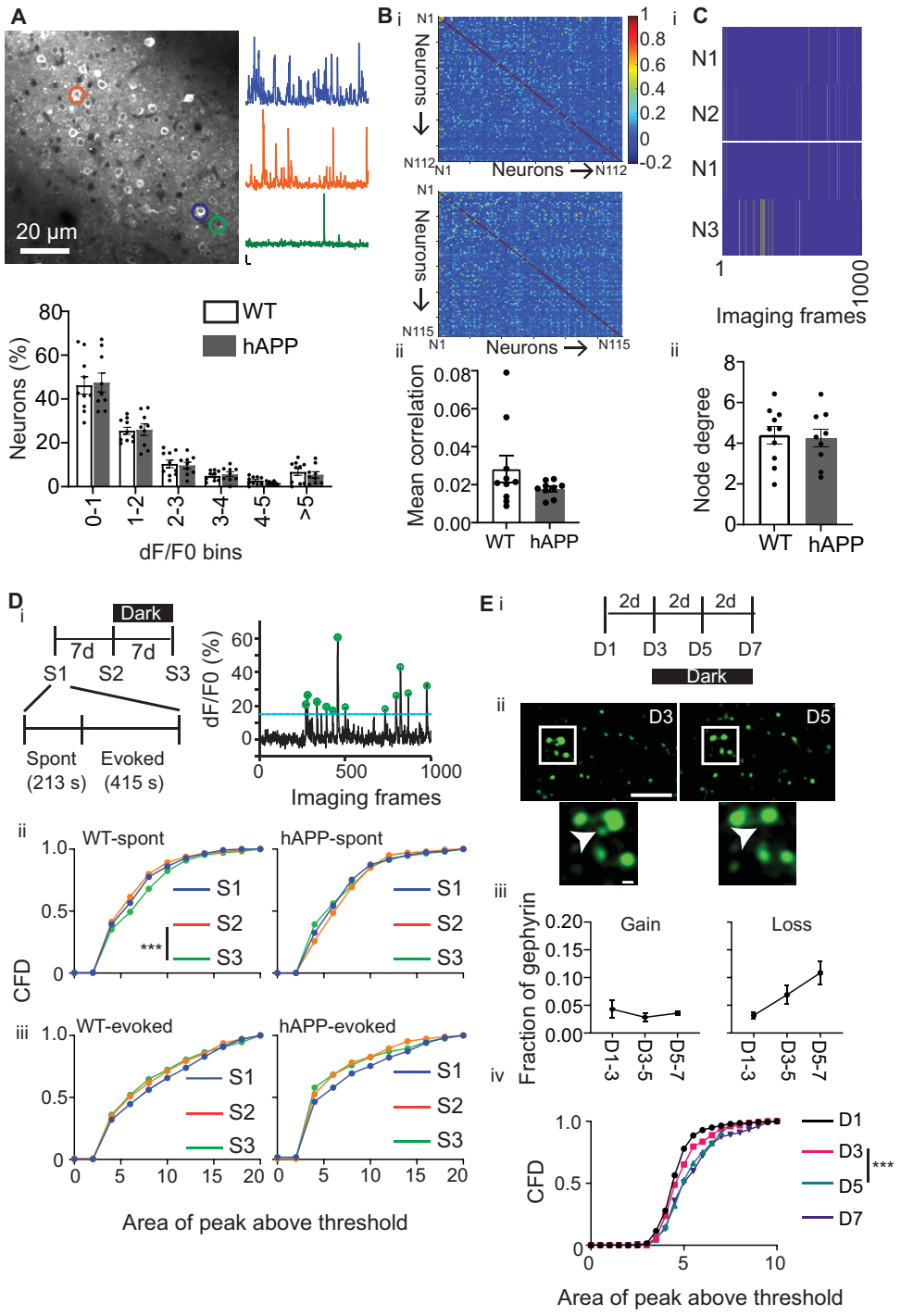

Figure 4. Baseline spontaneous activity is similar in WT and hAPP mice, whereas visual deprivation broadens it selectively in WT mice. ***A***, Standard deviation projection image of a r-epresentative imaging field of neurons expressing GCaMP6s (top). Calcium transients (dF/F0) of three color-matched circled neurons with varying levels of activity. Percentage of neurons in different dF/F0 bins in WT and hAPP mice (bottom). ***B***, (i) Representative correlation matrices of WT and hAPP mice. (ii) Mean correlation from all mice. ***C***, (i) Representative deconvolved spikes from two neurons that are functionally connected (top) or not connected (bottom). (ii) The average node degree. $n = 10$ WT (1,020 neurons) and 9 hAPP mice (885 neurons). Data are presented as mean ± SEM. Circles represent the average of each mouse. ***D***, (i, left) Experimental paradigm—S1, S2, and S3 are imaging sessions separated by 7 d. Between S2 and S3, mice were housed in darkness for 1 week. In each imaging session, both spontaneous (Spont) and visually evoked activities were imaged (indicated for S1). (Right) Calcium transients during spontaneous imaging frames of an example neuron. The blue line represents the mean + 2 standard deviation threshold above which peaks (marked by green circles) were detected. (ii–iii) Cumulative frequency distribution (CFD) of neurons with average AUC per peak above the threshold during spontaneous (ii) and evoked (iii) activities in WT (left) and hAPP (right) mice. $n = 390$ (S1), 401 (S2), and 419 (S3) WT neurons (5 WT mice) and 233 (S1), 206 (S2), and 209 (S3) hAPP neurons (4 hAPP mice). ***$p < 0.001$ Kolmogorov–Smirnov (KS) test. The alpha value was set to 0.025 to account for multiple (S1 vs S2 and S2 vs S3) comparisons (Bonferroni correction). ***E***, (i) Timeline of gephyrin and jRGECO imaging sessions separated by 2 d. Between day (D)3 and D7, mice were housed in complete darkness. (ii) Representative images of gephyrin puncta detected by GPHN-FingR-GFP on D3 and D5 (scale bar, 10 μm). The white box is magnified below, and the arrow points to a lost puncta (scale bar, 1 μm). (iii) Fraction of gephyrin puncta (total, 422 puncta) gained (left) and lost (right) between sessions. Gain did not significantly change over time, whereas loss increased [$p < 0.05$, $F_{(1.69,\ 8.46)} = 5.8$]; repeated-measures ANOVA for loss. $n = 6$ WT mice). (iv) CFD of neurons with average AUC per peak above the threshold of spontaneous calcium transients for each neuron. ***$p < 0.001$ Kolmogorov–Smirnov (KS) test. $n = 140$ (D1), 152 (D3), 165 (D5), and 122 (D7) neurons. The alpha value was set to 0.016 to account for multiple comparisons (D1 vs D3, D3 vs D5, D5 vs D7; Bonferroni correction).

grating stimuli and natural images interspersed with gray screen) calcium transients. Since inhibition regulates the temporal window of integration of synaptic excitation (Isaacson and Scanziani, 2011), we quantified the AUC of each calcium transient exceeding a threshold (peaks with dF/F0 greater than two standard deviations from mean dF/F0) during the entire spontaneous imaging period (~213 s). Similarly, we measured the AUC of calcium transients associated with visual stimuli (except gray screen) during the evoked imaging period. We observed that the CFD of the average AUC per transient for each neuron remained largely unchanged between the first two sessions for both spontaneous and evoked activities across both genotypes, though there was a nonsignificant left shift in evoked activity (Fig. 4*D*, ii and iii). Following visual deprivation (between the second and third sessions), we detected a subtle but significant (Kolmogorov–Smirnov $D = 0.14$, $p < 0.001$) shift toward the right in the frequency distribution of the average AUC per transient of spontaneous activity in WT mice but not in hAPP mice (Fig. 4*D*, ii). The right shift in the frequency distribution following visual deprivation in WT mice persisted even if we changed the threshold for peak detection to three standard deviations from the mean (Kolmogorov–Smirnov $D = 0.11$, $p = 0.015$). The small increase in spontaneous activity observed after visual deprivation in WT mice is consistent with previous reports showing a subtle increase in spontaneous activity in visual and auditory cortices following dark exposure (Bridi et al., 2018; Solarana et al., 2019). In contrast to spontaneous activity, the frequency distribution of visually evoked AUC per transient in both genotypes did not show any significant alterations due to visual deprivation (Fig. 4*D*, iii). This indicates that the evoked activity was largely unaffected by the deprivation. These results show that spontaneous neural activity, similar to inhibitory synapse loss, is elevated following 1 week of dark housing in WT but not hAPP mice. These results are also consistent with our recent findings that c-Fos expression in the visual cortex is increased in WT but not hAPP mice following 1 week of dark exposure (L'Esperance et al., 2023).

To further refine the time course of inhibitory synapse loss and increased spontaneous neuronal activity in WT mice, we labeled inhibitory synapses with a GPHN.FingR-GFP (Gross et al., 2013), an intrabody that recognizes gephyrin, and neurons with jRGECO, a red fluorescent calcium sensor (Dana et al., 2016). We imaged spontaneous activity and gephyrin puncta (not in the same neurons) every 2 d for 6 d, with mice housed in complete darkness for the last 4 d (Fig. 4*E*, i). Between the first two sessions, when mice were housed in the normal light/dark cycle, the fraction of inhibitory synapses gained (0.04 ± 0.02) and lost (0.03 ± 0.01) was similar (Fig. 4*E*, ii and iii). However, the loss was higher than the gain after 2 d in the dark (gain, 0.03 ± 0.01; loss, 0.07 ± 0.02; $p = 0.09$, paired t test) but reached significance when tested after 4 d in the dark (gain, 0.04 ± 0.01; loss, 0.10 ± 0.02; $p = 0.01$, paired t test; Fig. 4*E*, iii). We found that the broadening of spontaneous calcium transients occurred during the first 2 d of complete darkness, and no further broadening occurred during the next 2 d in darkness (Fig. 4*E*), indicating that the structural loss of gephyrin may serve to stabilize functional changes.

Disrupted clustering of excitatory and inhibitory synapse loss in amyloidosis

The visual deprivation paradigm allowed us to identify a deficit in the loss of inhibitory synapses in amyloid pathology. However, it remains unclear whether amyloid pathology interferes with or alters compensatory inhibitory changes under normal conditions. Excitatory and inhibitory synapses are known to exhibit structural plasticity and tend to cluster spatially (Chen et al., 2012). We hypothesized that if inhibitory synapses do not respond to changes in excitatory synaptic activity, the loss of excitatory synapses might not be associated with a local loss of inhibitory synapses in hAPP mice, even under normal visual conditions (12 h light cycle).

To test this, we measured the nearest neighbor distances from each lost excitatory synapse (source synapse) to lost inhibitory synapses (target synapses) under normal visual conditions (Fig. 5*A*). The median and mean distances in WT mice were 4 and 6.8 ± 1.2 µm, respectively. These distances were significantly greater in hAPP mice, with median and mean values of 7.7 and 13.2 ± 2.1 µm, respectively (Fig. 5*A*).

We implemented a randomization procedure to determine whether observed clustering distances reflect changes in the synapse density and number of lost synapses within a dendritic segment between genotypes. We simulated the loss of excitatory synapses using experimentally observed locations. For each experimentally observed lost excitatory synapse (source) within the dendritic segment, we iteratively randomized the locations and loss positions of the inhibitory synapses (target) 10,000 times. We calculated the nearest neighbor distances for each iteration. This randomization process was performed for every experimentally identified lost excitatory synapse, and the resulting distances were averaged to generate a random distribution for comparison with the observed data. The observed mean nearest neighbor distance of lost excitatory (source) and inhibitory (target) synapses for WT mice was significantly lower than the randomized distribution (WT-randomized, 9.0 ± 1.3 µm; hAPP-randomized, 15.1 ± 2.2 µm for hAPP). However, the median distances of the randomized distributions (WT-randomized, 8.9 ± 1.3 µm; hAPP-randomized, 14.9) were greater than the observed medians for both genotypes, suggesting that local clustering is disrupted for some lost excitatory synapses in hAPP mice (Fig. 5*A*).

We next examined whether similar changes to local clustering occur if lost inhibitory synapses are used as a reference point (source) to identify nearest neighbor distances of lost excitatory synapses (target). We found that the distribution of nearest neighbor distances between inhibitory synapses (source) and excitatory synapses (target) in both WT and hAPP mice did not show any significant differences. Furthermore, their mean was not significantly different from the random distribution (Fig. 5*B*). However, the median distance between the lost inhibitory and excitatory synapses was found to be lower than that of the random distribution. Specifically, the median values were 9.4 µm for WT and 11 µm for hAPP, compared to 16.1 µm for WT-randomized and 19.2 µm for hAPP-randomized. These results indicate that the spatial relationship between lost inhibitory and excitatory synapses is not entirely random, and there are instances where they are closer to each other than would be expected by chance.

To further confirm that the closer clustering of inhibitory synapse loss to lost excitatory synapses in WT compared to hAPP mice (Fig. 5*A*) is not a reflection of spacing between excitatory and inhibitory synapses in these genotypes, we first measured the nearest neighbor distances of inhibitory synapses (target) to every excitatory synapse (source). We found they were very similar (median WT, 1.04 µm; hAPP, 0.96 µm; Fig. 5*C*) between the genotypes. We also examined the distribution of nearest neighbor distances of lost excitatory synapses to each other and found the mean to be 14.8 ± 2.2 µm for WT and 17.9 ± 3.2 µm for

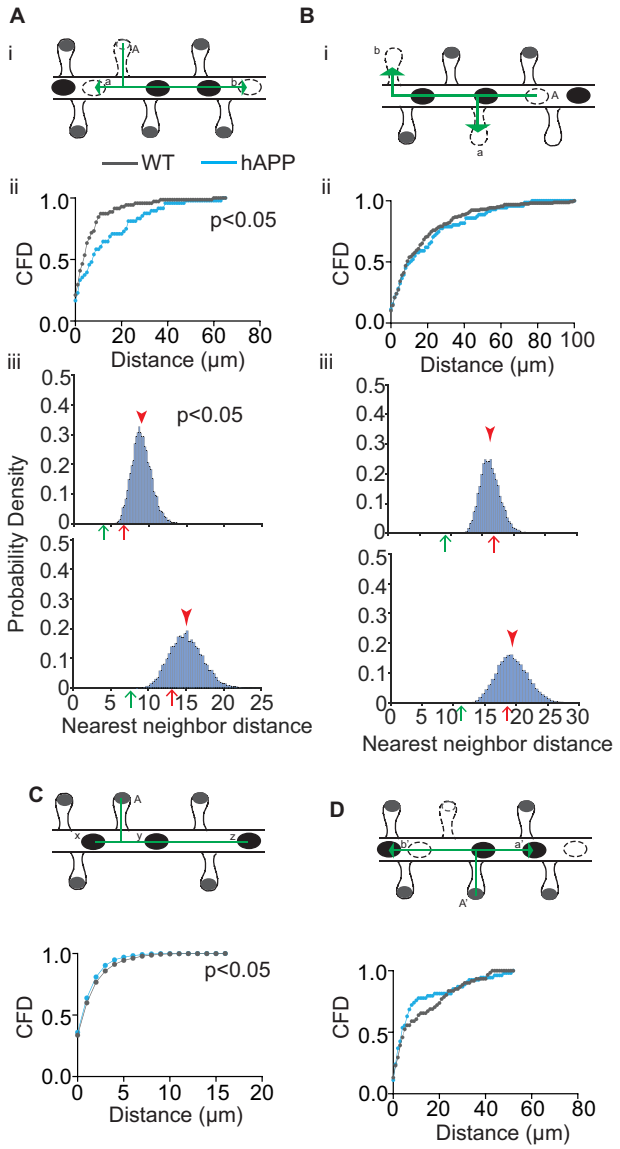

Figure 5. Local clustering of excitatory and inhibitory synapse loss is disrupted in hAPP mice. ***A***, (i) A representative illustration of nearest neighbor analysis. "A" is an excitatory synapse that disappeared between imaging sessions. "a" and "b" are two inhibitory synapses that disappeared during the same interval. "a" will be the nearest inhibitory synapse loss (target) for the lost excitatory synapse "A" (source) in this dendritic segment. The distance to the nearest inhibitory synapse loss was calculated for every excitatory synapse lost. (ii) CFD of nearest neighbor distances of inhibitory synapse loss to lost excitatory synapses. $n = 71$ (WT) and 48 (hAPP) lost excitatory synapses, $p < 0.05$, Kolmogorov–Smirnov (KS) test. (iii) Distribution of average nearest neighbor distances of randomized inhibitory synapse loss to all experimentally observed locations of excitatory synapse loss from all dendrites in WT (top) and hAPP (bottom). Red arrowhead, red arrow, and green arrow indicate the mean of random distribution, mean, and median observed values, respectively. $p < 0.05$ (*Z* test, left-sided). ***B***, (i) "a" is the nearest excitatory synapse lost (target) to "A," a lost inhibitory synapse (source). (ii) CFD of nearest neighbor distances of excitatory synapse loss to lost inhibitory synapses. $n = 158$ (WT) and 71 (hAPP) lost inhibitory synapses. (iii) Distribution of average nearest neighbor distances of randomized excitatory synapse loss to all experimentally observed locations of inhibitory synapse loss from all dendrites in WT (top) and hAPP (bottom). The red arrowhead indicates the mean of random distribution. ***C***, (Top) "x" is the nearest inhibitory synapse (target) to "A," the excitatory synapse (source). (Bottom) CFD of nearest neighbor distances of inhibitory synapses to all excitatory synapses. $p < 0.05$ Kolmogorov–Smirnov (KS) test, $n = 2,453$ (WT) and 1,851 (hAPP) excitatory synapses. ***D***, (Top) a' is the nearest gained inhibitory synapse (target) to A', a gained excitatory synapse (source) between sessions. For every gained excitatory synapse, the distance to the nearest inhibitory synapse gain was calculated. (Bottom) CFD of nearest neighbor distances of gained inhibitory synapses (target) to all gained excitatory synapses (source). $n = 61$ (WT) and 54 (hAPP) gained excitatory synapses.

hAPP. The median values were 8.9 μm for WT and 10.3 μm for hAPP. Similarly, for lost inhibitory synapses, the mean nearest neighbor distances with each other were 8.6 ± 0.8 μm for WT and 10.1 ± 0.9 μm for hAPP, with median values of 4.4 μm for WT and 6.0 μm for hAPP. These measurements indicate that the distribution of nearest neighbor distances when the target and source synapse types are the same were not significantly different between the genotypes.

When we compared the distribution of the nearest neighbor distances of gained inhibitory synapses (target) in relation to gained excitatory synapses (source), we did not observe a significant difference between the genotypes (Fig. 5*D*). Both genotypes demonstrated close clustering, with median values of 5 μm for WT and 4 μm for hAPP. Together, these results show that the right shift in the distribution of the nearest neighbor distances of lost excitatory and inhibitory synapses in hAPP mice represents an impairment in their local clustering.

Discussion

Direct visualization of synaptic proteins in vivo, repeated imaging of the same synapses, and the use of the visual cortex as a model system, which is amenable to altering experience-evoked activity, allowed us to unearth a pathological feature of amyloid that would not be directly evident by visualizing the density or baseline dynamics of synapses either in vitro or in vivo. Multiple animal studies have uncovered the vulnerability of the visual cortex to AD-related pathology and subtle synaptic dysfunction without overt degeneration could contribute to visual deficits observed in a subset of AD patients (Armstrong, 1996; Grienberger et al., 2012; William et al., 2012, 2021; Liebscher et al., 2016; Korzhova et al., 2021; Kurucu et al., 2022; Papanikolaou et al., 2022; Niraula et al., 2023).

In amyloid pathology, we identified a selective disruption in the experience-dependent structural adaptation of inhibitory synapses on the dendritic shaft. The density or baseline structural dynamics of inhibitory synapses were not significantly perturbed. Furthermore, the baseline structural dynamics of excitatory synapses and their response to altered experience remain unchanged in the same neurons. These results indicate that structural plasticity deficits in the inhibitory system emerge before impairments in the structural plasticity of excitatory synapses in amyloidosis.

Hyper- and hypoactivity of neurons and brain regions in AD are thought to arise due to defective homeostatic adaptation (Jang and Chung, 2016; Frere and Slutsky, 2018; Styr and Slutsky, 2018). Excitatory synapse loss is thought to be one of the maladaptive plasticity mechanisms to restrain hyperactivity and could lead to hypoactivity when unchecked (Styr and Slutsky, 2018). A reduction in excitatory synapse density and brain activity is observed in the later stages of AD (Terry et al., 1991; DeKosky et al., 1996; Dickerson et al., 2005; Celone et al., 2006; Scheff and Price, 2006), indicating disrupted inhibitory plasticity mechanisms may underlie lack of compensation to the reduced neural activity associated with excitatory synapse loss. Though the order of emergence of hyper- and hypoactivity is still unclear, they must closely follow each other to maintain average activity levels as the total energy budget of the brain is fixed (Herculano-Houzel, 2011). Consistently, hyper- and hypoactive neurons are present together in mouse models of amyloidosis (Busche et al., 2008; Grienberger et al., 2012; Rudinskiy et al., 2012; Niraula et al., 2023). We recently observed that the increase in neuronal hyper- and hypoactivity occurs at a stage where postsynaptic densities of excitatory and inhibitory

synapses are comparable to nonpathological controls (Niraula et al., 2023). Therefore, mechanisms other than excitatory synapse loss, such as changes to the size, stability, and physiology of inhibitory synapses, may contribute to hypoactivity. Consistently, gephyrin levels were found to be higher in amyloid pathology (Hales et al., 2013; Kiss et al., 2016), though the literature is inconsistent on the direction of change in the GABAergic system concerning favoring or opposing hyperactivity. The insensitivity of inhibitory synapses to activity perturbation and local decoupling of excitatory and inhibitory synapse loss indicates that inhibitory synapses in amyloid pathology may not compensate for the reduction in activity levels.

In line with the role of inhibitory synapse plasticity in maintaining neuronal activity homeostasis, synaptic inhibition is increased in the light phase of the light/dark cycle to compensate for increased excitability in the dark phase (Bridi et al., 2020). Consistently, neurons in the visual cortex do not exhibit significant activity changes across light/dark cycles (Torrado Pacheco et al., 2019). However, 2 d dark exposure elicits disinhibition (Huang et al., 2015), and increased spontaneous activity has been observed after 1 week (Bridi et al., 2018). We also observed that the average AUC of calcium transients per neuron increased following dark exposure in WT but not hAPP mice, which also do not exhibit increased inhibitory synapse loss. However, increased inhibitory synapse loss continued to persist beyond 2 d of dark exposure, whereas the increase in AUC of spontaneous calcium transient did not. The functional shift in neural activity may be caused by visual deprivation-mediated changes to GABA and glutamate receptors (Yashiro, Corlew and Philpot, 2005; He, Hodos and Quinlan, 2006; Goel and Lee, 2007). The structural loss of gephyrin could make this change more permanent, such that GABA receptors are not recruited back to the gephyrin scaffold. Alternatively, calcium transient broadening may have a ceiling effect and could not increase with ongoing structural loss of inhibitory synapses.

Intriguingly, we did not observe an increase in the AUC of calcium transients for visually evoked activity, indicating inhibitory synapse loss associated with long-term dark exposure may modulate nonvisual inputs. In this view, inhibitory synapse loss may not serve a homeostatic role and may promote plasticity by increasing the temporal window of synaptic activity during each calcium transient. Since dendritic disinhibition promotes learning-associated plasticity (Letzkus et al., 2015; Mohler and Rudolph, 2017; Artinian and Lacaille, 2018; Wu et al., 2022), disrupted inhibitory synapse adaptation may also interfere with learning or cross-modal plasticity in amyloidosis. Though the direction of neural activity and inhibitory synaptic plasticity in both genotypes are consistent, it is challenging to extrapolate the small effect size of structural synaptic changes to neural and microcircuit activity.

Disrupted inhibitory synapse loss following visual deprivation in hAPP mice may arise due to multiple mechanisms. There may be no intrinsic defect in inhibitory synapses that prevents them from undergoing synapse loss. For instance, an elevated baseline activity may not necessitate inhibitory synapse loss in hAPP mice. However, our spontaneous activity analyses indicate that baseline spontaneous activity (without visual experience) in the visual cortex of hAPP mice at this age is similar to nonpathological controls based on multiple metrics. Therefore, impaired inhibitory synapse adaptation is unlikely due to higher spontaneous activity in hAPP mice in the dark. Alternatively, the neurons in hAPP mice may lack sensors to detect changes in activity. We found that excitatory synapses respond to visual deprivation by reducing ongoing spine gain in the neurons exhibiting inhibitory synapse loss deficits. This argues against a general defect in sensing reduction in activity levels. We propose that at least a fraction of inhibitory synapses in neurons of hAPP mice become disengaged from changes in excitatory activity. As a result, these synapses are more stabilized, and local alteration in an excitatory activity does not destabilize them.

Is inhibitory synapse loss a response to or a cause of excitatory synapse loss? The clustered loss of excitatory and inhibitory synapses is disrupted in hAPP mice only when the proximity of inhibitory synapse loss (target) to lost excitatory synapses (source) was measured. The distance of the nearest excitatory synapse loss (target) to lost inhibitory synapses (source) is larger and did not differ between hAPP and WT mice. These results suggest that inhibitory synapses in amyloidosis are deficient in sensing or responding to changes in excitatory activity. The mechanisms that drive inhibitory synapse loss following excitatory synapse loss are unclear. Multiple signaling pathways have been shown to enhance or weaken inhibitory synapses following enhancement in excitation (Rutherford et al., 1997; Swanwick et al., 2006; Chen et al., 2012; Flores et al., 2015; Hu et al., 2019; Ravasenga et al., 2022). It is unclear whether these signaling mechanisms also weaken inhibitory synapses following the weakening of excitatory synapses, possibly by maintaining their co-stability. The direction of clustering of excitatory synapse and inhibitory synapse gain or loss may differ depending on the context. In the learning context, disinhibition is favorable, and consistently, an increase in excitatory synaptic strength was shown to weaken inhibitory synaptic strength within 3 μm (Ravasenga et al., 2022). Our study differs from this study since we looked at clustering of excitatory and inhibitory synapse loss, but interestingly, the median distance (4 μm) of clustering was very similar in WT mice. The reduction in local clustering of excitatory and inhibitory synapse loss may be a consequence of the increased stability of gephyrin from degradation. Multiple posttranslational modifications, particularly phosphorylation, influence gephyrin stability (Tyagarajan et al., 2011; Kuhse et al., 2012; Kalbouneh et al., 2014; Zacchi et al., 2014; Flores et al., 2015; Wang et al., 2015; Zhou et al., 2021). Kinases that phosphorylate gephyrin and alter its stability, such as CDK5, are dysregulated in AD (Kiss et al., 2020). Whether CDK5-mediated phosphorylation or other posttranslational mechanisms are involved in disrupted disinhibition remains to be tested.

Visual deprivation has been shown to elicit rapid disinhibition due to reduced activity of parvalbumin-expressing interneurons (Hengen et al., 2013; Kuhlman et al., 2013; Barnes et al., 2015). Parvalbumin-expressing neurons primarily target perisomatic regions and proximal dendrites, whereas somatostatin-expressing interneurons target distal dendrites (Di Cristo et al., 2004). However, their localization is not mutually exclusive. We did not find a spatially restricted dendritic disinhibition, and the reduction of synapse density by deprivation appeared to be more uniform across the length of the dendrite. Future work with cell type-specific labeling is required to test whether structural disinhibition happens at both parvalbumin and somatostatin innervations.

References

Armstrong RA (1996) Visual field defects in Alzheimer's disease patients may reflect differential pathology in the primary visual cortex. Optom Vis Sci 73:677–682.

Artinian J, Lacaille JC (2018) Disinhibition in learning and memory circuits: new vistas for somatostatin interneurons and long-term synaptic plasticity. Brain Res Bull 141:20–26.

Barnes SJ, Franzoni E, Jacobsen RI, Erdelyi F, Szabo G, Clopath C, Keller GB, Keck T (2017) Deprivation-induced homeostatic spine scaling *in vivo* is localized to dendritic branches that have undergone recent spine loss. Neuron 96:871–882 e875.

Barnes SJ, Sammons RP, Jacobsen RI, Mackie J, Keller GB, Keck T (2015) Subnetwork-specific homeostatic plasticity in mouse visual cortex *in vivo*. Neuron 86:1290–1303.

Bridi MCD, et al. (2018) Two distinct mechanisms for experience-dependent homeostasis. Nat Neurosci 21:843–850.

Bridi MCD, et al. (2020) Daily oscillation of the excitation-inhibition balance in visual cortical circuits. Neuron 105:621–629 e624.

Busche MA, Eichhoff G, Adelsberger H, Abramowski D, Wiederhold KH, Haass C, Staufenbiel M, Konnerth A, Garaschuk O (2008) Clusters of hyperactive neurons near amyloid plaques in a mouse model of Alzheimer's disease. Science 321:1686–1689.

Busche MA, Konnerth A (2016) Impairments of neural circuit function in Alzheimer's disease. Philos Trans R Soc Lond B Biol Sci 371.

Celone KA, et al. (2006) Alterations in memory networks in mild cognitive impairment and Alzheimer's disease: an independent component analysis. J Neurosci 26:10222–10231.

Chen TW, et al. (2013) Ultrasensitive fluorescent proteins for imaging neuronal activity. Nature 499:295–300.

Chen L, Li X, Tjia M, Thapliyal S (2022) Homeostatic plasticity and excitation-inhibition balance: The good, the bad, and the ugly. Curr Opin Neurobiol 75:102553.

Chen JL, Villa KL, Cha JW, So PT, Kubota Y, Nedivi E (2012) Clustered dynamics of inhibitory synapses and dendritic spines in the adult neocortex. Neuron 74:361–373.

Coleman JE, Nahmani M, Gavornik JP, Haslinger R, Heynen AJ, Erisir A, Bear MF (2010) Rapid structural remodeling of thalamocortical synapses parallels experience-dependent functional plasticity in mouse primary visual cortex. J Neurosci 30:9670–9682.

Dana H, et al. (2016) Sensitive red protein calcium indicators for imaging neural activity. Elife 5:e12727.

DeKosky ST, Scheff SW, Styren SD (1996) Structural correlates of cognition in dementia: quantification and assessment of synapse change. Neurodegeneration 5:417–421.

Dickerson BC, et al. (2005) Increased hippocampal activation in mild cognitive impairment compared to normal aging and AD. Neurology 65:404–411.

Di Cristo G, Wu C, Chattopadhyaya B, Ango F, Knott G, Welker E, Svoboda K, Huang ZJ (2004) Subcellular domain-restricted GABAergic innervation in primary visual cortex in the absence of sensory and thalamic inputs. Nat Neurosci 7:1184–1186.

Dorostkar MM, Zou C, Blazquez-Llorca L, Herms J (2015) Analyzing dendritic spine pathology in Alzheimer's disease: problems and opportunities. Acta Neuropathol 130:1–19.

Flores CE, Nikonenko I, Mendez P, Fritschy JM, Tyagarajan SK, Muller D (2015) Activity-dependent inhibitory synapse remodeling through gephyrin phosphorylation. Proc Natl Acad Sci U S A 112:E65–72.

Fortin DA, et al. (2014) Live imaging of endogenous PSD-95 using ENABLED: a conditional strategy to fluorescently label endogenous proteins. J Neurosci 34:16698–16712.

Frere S, Slutsky I (2018) Alzheimer's disease: from firing instability to homeostasis network collapse. Neuron 97:32–58.

Gainey MA, Feldman DE (2017) Multiple shared mechanisms for homeostatic plasticity in rodent somatosensory and visual cortex. Philos Trans R Soc Lond B Biol Sci 372.

Garcia-Marin V, Blazquez-Llorca L, Rodriguez JR, Boluda S, Muntane G, Ferrer I, Defelipe J (2009) Diminished perisomatic GABAergic terminals on cortical neurons adjacent to amyloid plaques. Front Neuroanat 3:28.

Goel A, Lee HK (2007) Persistence of experience-induced homeostatic synaptic plasticity through adulthood in superficial layers of mouse visual cortex. J Neurosci 27:6692–6700.

Grienberger C, Rochefort NL, Adelsberger H, Henning HA, Hill DN, Reichwald J, Staufenbiel M, Konnerth A (2012) Staged decline of neuronal function in vivo in an animal model of Alzheimer's disease. Nat Commun 3:774.

Gross GG, et al. (2013) Recombinant probes for visualizing endogenous synaptic proteins in living neurons. Neuron 78:971–985.

Hales CM, et al. (2013) Abnormal gephyrin immunoreactivity associated with Alzheimer disease pathologic changes. J Neuropathol Exp Neurol 72: 1009–1015.

Harris JA, Devidze N, Halabisky B, Lo I, Thwin MT, Yu GQ, Bredesen DE, Masliah E, Mucke L (2010) Many neuronal and behavioral impairments in transgenic mouse models of Alzheimer's disease are independent of caspase cleavage of the amyloid precursor protein. J Neurosci 30:372–381.

He HY, Hodos W, Quinlan EM (2006) Visual deprivation reactivates rapid ocular dominance plasticity in adult visual cortex. J Neurosci 26:2951–2955.

Hengen KB, Lambo ME, Van Hooser SD, Katz DB, Turrigiano GG (2013) Firing rate homeostasis in visual cortex of freely behaving rodents. Neuron 80:335–342.

Herculano-Houzel S (2011) Scaling of brain metabolism with a fixed energy budget per neuron: implications for neuronal activity, plasticity and evolution. PLoS One 6:e17514.

Hofer SB, Mrsic-Flogel TD, Bonhoeffer T, Hubener M (2009) Experience leaves a lasting structural trace in cortical circuits. Nature 457:313–317.

Hollnagel JO, Elzoheiry S, Gorgas K, Kins S, Beretta CA, Kirsch J, Kuhse J, Kann O, Kiss E (2019) Early alterations in hippocampal perisomatic GABAergic synapses and network oscillations in a mouse model of Alzheimer's disease amyloidosis. PLoS One 14:e0209228.

Hu HY, Kruijssen DLH, Frias CP, Rozsa B, Hoogenraad CC, Wierenga CJ (2019) Endocannabinoid signaling mediates local dendritic coordination between excitatory and inhibitory synapses. Cell Rep 27:666–675 e665.

Huang S, Hokenson K, Bandyopadhyay S, Russek SJ, Kirkwood A (2015) Brief dark exposure reduces tonic inhibition in visual cortex. J Neurosci 35: 15916–15920.

Isaacson JS, Scanziani M (2011) How inhibition shapes cortical activity. Neuron 72:231–243.

Jang SS, Chung HJ (2016) Emerging link between Alzheimer's disease and homeostatic synaptic plasticity. Neural Plast 2016:7969272.

Jimenez-Balado J, Eich TS (2021) GABAergic dysfunction, neural network hyperactivity and memory impairments in human aging and Alzheimer's disease. Semin Cell Dev Biol 116:146–159.

Kalbouneh H, Schlicksupp A, Kirsch J, Kuhse J (2014) Cyclin-dependent kinase 5 is involved in the phosphorylation of gephyrin and clustering of GABAA receptors at inhibitory synapses of hippocampal neurons. PLoS One 9:e104256.

Keck T, Keller GB, Jacobsen RI, Eysel UT, Bonhoeffer T, Hubener M (2013) Synaptic scaling and homeostatic plasticity in the mouse visual cortex in vivo. Neuron 80:327–334.

Keck T, Mrsic-Flogel TD, Vaz Afonso M, Eysel UT, Bonhoeffer T, Hubener M (2008) Massive restructuring of neuronal circuits during functional reorganization of adult visual cortex. Nat Neurosci 11:1162–1167.

Keck T, Scheuss V, Jacobsen RI, Wierenga CJ, Eysel UT, Bonhoeffer T, Hubener M (2011) Loss of sensory input causes rapid structural changes of inhibitory neurons in adult mouse visual cortex. Neuron 71:869–882.

Kiss E, Gorgas K, Schlicksupp A, Gross D, Kins S, Kirsch J, Kuhse J (2016) Biphasic alteration of the inhibitory synapse scaffold protein gephyrin in early and late stages of an Alzheimer disease model. Am J Pathol 186:2279–2291.

Kiss E, Groeneweg F, Gorgas K, Schlicksupp A, Kins S, Kirsch J, Kuhse J (2020) Amyloid-beta fosters p35/CDK5 signaling contributing to changes of inhibitory synapses in early stages of cerebral amyloidosis. J Alzheimers Dis 74:1167–1187.

Korzhova V, Marinkovic P, Njavro JR, Goltstein PM, Sun F, Tahirovic S, Herms J, Liebscher S (2021) Long-term dynamics of aberrant neuronal activity in awake Alzheimer's disease transgenic mice. Commun Biol 4: 1368.

Kuhlman SJ, Olivas ND, Tring E, Ikrar T, Xu X, Trachtenberg JT (2013) A disinhibitory microcircuit initiates critical-period plasticity in the visual cortex. Nature 501:543–546.

Kuhse J, Kalbouneh H, Schlicksupp A, Mukusch S, Nawrotzki R, Kirsch J (2012) Phosphorylation of gephyrin in hippocampal neurons by cyclin-dependent kinase CDK5 at Ser-270 is dependent on collybistin. J Biol Chem 287:30952–30966.

Kurucu H, Colom-Cadena M, Davies C, Wilkins L, King D, Rose J, Tzioras M, Tulloch JH, Smith C, Spires-Jones TL (2022) Inhibitory synapse loss and accumulation of amyloid beta in inhibitory presynaptic terminals in Alzheimer's disease. Eur J Neurol 29:1311–1323.

Lee HK, Kirkwood A (2019) Mechanisms of homeostatic synaptic plasticity *in vivo*. Front Cell Neurosci 13:520.

L'Esperance OJ, McGhee J, Davidson G, Smith A, Niraula S, Subramanian J (2023) Functional connectivity favors aberrant visual network c-Fos expression accompanied by cortical synapse loss in amyloidosis. bioRxiv.

Letzkus JJ, Wolff SB, Luthi A (2015) Disinhibition, a circuit mechanism for associative learning and memory. Neuron 88:264–276.

Liebscher S, Keller GB, Goltstein PM, Bonhoeffer T, Hubener M (2016) Selective persistence of sensorimotor mismatch signals in visual cortex of behaving Alzheimer's disease mice. Curr Biol 26:956–964.
Liebscher S, Meyer-Luehmann M (2012) A peephole into the brain: neuropathological features of Alzheimer's disease revealed by *in vivo* two-photon imaging. Front Psychiatry 3:26.
Melgosa-Ecenarro L, Doostdar N, Radulescu CI, Jackson JS, Barnes SJ (2023) Pinpointing the locus of GABAergic vulnerability in Alzheimer's disease. Semin Cell Dev Biol 139:35–54.
Mitew S, Kirkcaldie MT, Dickson TC, Vickers JC (2013) Altered synapses and gliotransmission in Alzheimer's disease and AD model mice. Neurobiol Aging 34:2341–2351.
Mohler H, Rudolph U (2017) Disinhibition, an emerging pharmacology of learning and memory. F1000Res 6.
Montero-Crespo M, Dominguez-Alvaro M, Alonso-Nanclares L, DeFelipe J, Blazquez-Llorca L (2021) Three-dimensional analysis of synaptic organization in the hippocampal CA1 field in Alzheimer's disease. Brain 144: 553–573.
Niraula S, Doderer JJ, Indulkar S, Berry KP, Hauser WL, L'Esperance OJ, Deng JZ, Keeter G, Rouse AG, Subramanian J (2023) Excitation-inhibition imbalance disrupts visual familiarity in amyloid and non-pathology conditions. Cell Rep 42:111946.
O'Brien JL, O'Keefe KM, LaViolette PS, DeLuca AN, Blacker D, Dickerson BC, Sperling RA (2010) Longitudinal fMRI in elderly reveals loss of hippocampal activation with clinical decline. Neurology 74:1969–1976.
Pachitariu M, Stringer C, Dipoppa M, Schröder S, Rossi LF, Dalgleish H, Carandini M, Harris KD (2017) Suite2p: beyond 10,000 neurons with standard two-photon microscopy. bioRxiv.
Palop JJ, Mucke L (2016) Network abnormalities and interneuron dysfunction in Alzheimer disease. Nat Rev Neurosci 17:777–792.
Palop JJ, Mucke L, Roberson ED (2011) Quantifying biomarkers of cognitive dysfunction and neuronal network hyperexcitability in mouse models of Alzheimer's disease: depletion of calcium-dependent proteins and inhibitory hippocampal remodeling. Methods Mol Biol 670:245–262.
Papanikolaou A, Rodrigues FR, Holeniewska J, Phillips KG, Saleem AB, Solomon SG (2022) Plasticity in visual cortex is disrupted in a mouse model of tauopathy. Commun Biol 5:77.
Petrache AL, Rajulawalla A, Shi A, Wetzel A, Saito T, Saido TC, Harvey K, Ali AB (2019) Aberrant excitatory-inhibitory synaptic mechanisms in entorhinal cortex microcircuits during the pathogenesis of Alzheimer's disease. Cereb Cortex 29:1834–1850.
Ravasenga T, Ruben M, Regio V, Polenghi A, Petrini EM, Barberis A (2022) Spatial regulation of coordinated excitatory and inhibitory synaptic plasticity at dendritic synapses. Cell Rep 38:110347.
Rudinskiy N, Hawkes JM, Betensky RA, Eguchi M, Yamaguchi S, Spires-Jones TL, Hyman BT (2012) Orchestrated experience-driven Arc responses are disrupted in a mouse model of Alzheimer's disease. Nat Neurosci 15: 1422–1429.
Ruiter M, Herstel LJ, Wierenga CJ (2020) Reduction of dendritic inhibition in CA1 pyramidal neurons in amyloidosis models of early Alzheimer's disease. J Alzheimers Dis 78:951–964.
Ruiter M, Lutzkendorf C, Liang J, Wierenga CJ (2021) Amyloid-beta oligomers induce only mild changes to inhibitory bouton dynamics. J Alzheimers Dis Rep 5:153–160.
Rutherford LC, DeWan A, Lauer HM, Turrigiano GG (1997) Brain-derived neurotrophic factor mediates the activity-dependent regulation of inhibition in neocortical cultures. J Neurosci 17:4527–4535.
Salinas E, Sejnowski TJ (2001) Correlated neuronal activity and the flow of neural information. Nat Rev Neurosci 2:539–550.
Sammons RP, Clopath C, Barnes SJ (2018) Size-dependent axonal bouton dynamics following visual deprivation *in vivo*. Cell Rep 22:576–584.
Scaduto P, et al. (2023) Functional excitatory to inhibitory synaptic imbalance and loss of cognitive performance in people with Alzheimer's disease neuropathologic change. Acta Neuropathol 145:303–324.
Scheff SW, Price DA (2006) Alzheimer's disease-related alterations in synaptic density: neocortex and hippocampus. J Alzheimers Dis 9:101–115.
Schmid LC, et al. (2016) Dysfunction of somatostatin-positive interneurons associated with memory deficits in an Alzheimer's disease model. Neuron 92:114–125.
Shimojo M, et al. (2020) Selective disruption of inhibitory synapses leading to neuronal hyperexcitability at an early stage of tau pathogenesis in a mouse model. J Neurosci 40:3491–3501.
Solarana K, Liu J, Bowen Z, Lee HK, Kanold PO (2019) Temporary visual deprivation causes decorrelation of spatiotemporal population responses in adult mouse auditory cortex. eNeuro 6.
Sos KE, et al. (2020) Amyloid beta induces interneuron-specific changes in the hippocampus of APPNL-F mice. PLoS One 15:e0233700.
Styr B, Slutsky I (2018) Imbalance between firing homeostasis and synaptic plasticity drives early-phase Alzheimer's disease. Nat Neurosci 21:463–473.
Subramanian J, Dye L, Morozov A (2013) Rap1 signaling prevents L-type calcium channel-dependent neurotransmitter release. J Neurosci 33:7245–7252.
Subramanian J, Michel K, Benoit M, Nedivi E (2019) CPG15/neuritin mimics experience in selecting excitatory synapses for stabilization by facilitating PSD95 recruitment. Cell Rep 28:1584–1595 e1585.
Subramanian J, Savage JC, Tremblay ME (2020) Synaptic loss in Alzheimer's disease: mechanistic insights provided by two-photon in vivo imaging of transgenic mouse models. Front Cell Neurosci 14:592607.
Sun YJ, Espinosa JS, Hoseini MS, Stryker MP (2019) Experience-dependent structural plasticity at pre- and postsynaptic sites of layer 2/3 cells in developing visual cortex. Proc Natl Acad Sci U S A 116:21812–21820.
Swanwick CC, Murthy NR, Kapur J (2006) Activity-dependent scaling of GABAergic synapse strength is regulated by brain-derived neurotrophic factor. Mol Cell Neurosci 31:481–492.
Targa Dias Anastacio H, Matosin N, Ooi L (2022) Neuronal hyperexcitability in Alzheimer's disease: what are the drivers behind this aberrant phenotype? Transl Psychiatry 12:257.
Terry RD, Masliah E, Salmon DP, Butters N, DeTeresa R, Hill R, Hansen LA, Katzman R (1991) Physical basis of cognitive alterations in Alzheimer's disease: synapse loss is the major correlate of cognitive impairment. Ann Neurol 30:572–580.
Torrado Pacheco A, Tilden EI, Grutzner SM, Lane BJ, Wu Y, Hengen KB, Gjorgjieva J, Turrigiano GG (2019) Rapid and active stabilization of visual cortical firing rates across light-dark transitions. Proc Natl Acad Sci U S A 116:18068–18077.
Tyagarajan SK, et al. (2011) Regulation of GABAergic synapse formation and plasticity by GSK3beta-dependent phosphorylation of gephyrin. Proc Natl Acad Sci U S A 108:379–384.
Umeda T, et al. (2017) Mutation-induced loss of APP function causes GABAergic depletion in recessive familial Alzheimer's disease: analysis of Osaka mutation-knockin mice. Acta Neuropathol Commun 5:59.
van Versendaal D, Rajendran R, Saiepour MH, Klooster J, Smit-Rigter L, Sommeijer JP, De Zeeuw CI, Hofer SB, Heimel JA, Levelt CN (2012) Elimination of inhibitory synapses is a major component of adult ocular dominance plasticity. Neuron 74:374–383.
Vardalaki D, Chung K, Harnett MT (2022) Filopodia are a structural substrate for silent synapses in adult neocortex. Nature 612:323–327.
Villa KL, Berry KP, Subramanian J, Cha JW, Oh WC, Kwon HB, Kubota Y, So PT, Nedivi E (2016) Inhibitory synapses are repeatedly assembled and removed at persistent sites *in vivo*. Neuron 89:756–769.
Wang CY, et al. (2015) Protein kinase C-dependent growth-associated protein 43 phosphorylation regulates gephyrin aggregation at developing GABAergic synapses. Mol Cell Biol 35:1712–1726.
William CM, Andermann ML, Goldey GJ, Roumis DK, Reid RC, Shatz CJ, Albers MW, Frosch MP, Hyman BT (2012) Synaptic plasticity defect following visual deprivation in Alzheimer's disease model transgenic mice. J Neurosci 32:8004–8011.
William CM, Stern MA, Pei X, Saqran L, Ramani M, Frosch MP, Hyman BT (2021) Impairment of visual cortical plasticity by amyloid-beta species. Neurobiol Dis 154:105344.
Wu YK, Miehl C, Gjorgjieva J (2022) Regulation of circuit organization and function through inhibitory synaptic plasticity. Trends Neurosci 45:884–898.
Yashiro K, Corlew R, Philpot BD (2005) Visual deprivation modifies both presynaptic glutamate release and the composition of perisynaptic/extrasynaptic NMDA receptors in adult visual cortex. J Neurosci 25:11684–11692.
Zacchi P, Antonelli R, Cherubini E (2014) Gephyrin phosphorylation in the functional organization and plasticity of GABAergic synapses. Front Cell Neurosci 8:103.
Zhou L, Kiss E, Demmig R, Kirsch J, Nawrotzki RA, Kuhse J (2021) Binding of gephyrin to microtubules is regulated by its phosphorylation at Ser270. Histochem Cell Biol 156:5–18.
Zhou Y, Lai B, Gan WB (2017) Monocular deprivation induces dendritic spine elimination in the developing mouse visual cortex. Sci Rep 7:4977.